

Uncertainties and Design of Active Aerodynamic Attitude Control in Very Low Earth Orbit

Sabrina Livadiotti^{*}, Nicholas H. Crisp[†], Peter C. E. Roberts[‡] and Vitor T. A. Oiko[§]
The University of Manchester, Oxford Road, Manchester, M13 9PL, United Kingdom

Simon Christensen[¶]
GomSpace A/S, Langagervej 6, 9220 Aalborg East, Denmark

Rosa Maria Domínguez^{||}
Elecnor Deimos Satellite Systems, Calle Francia 9, 13500 Puertollano, Spain

Georg H. Herdrich^{**}
Institute of Space Systems (IRS), University of Stuttgart, Pfaffenwaldring 29, 70569 Stuttgart, Germany

This paper discusses the design and the performance achievable with active aerodynamic attitude control in very low Earth orbit, i.e. below 450 km in altitude. A novel real-time algorithm is proposed for selecting the angles of deflection of aerodynamic actuators providing the closest match to the control signal computed by a selected control law. The algorithm is based on a panel method for the computation of the aerodynamic coefficients and relies on approximate environmental parameters estimation and worst-case scenario assumptions for the re-emission properties of space materials. Discussion of results is performed by assuming two representative pointing manoeuvres, for which momentum wheels and aerodynamic actuators are used synergistically. A quaternion feedback PID controller implemented in discrete time is assumed to determine the control signal at a sampling frequency of 1 Hz. The outcome of a Monte Carlo analysis, performed for a wide range of orbital conditions, shows that the target attitude is successfully achieved for the vast majority of the cases, thus proving the robustness of the approach in the presence of environmental uncertainties and realistic attitude hardware limitations.

Nomenclature

\mathbf{a}_A = aerodynamic acceleration vector

^{*}Corresponding author: Ph.D. Researcher, Department of MACE, sabrinativadiotti@gmail.com

[†]Postdoctoral Researcher, Department of MACE

[‡]Senior Lecturer, Department of MACE.

[§]Postdoctoral Researcher, Department of MACE

[¶]Systems Engineer

^{||}Physicist

^{**}Head Plasma Wind Tunnels and Electric Propulsion, IRS

$A_B^{p,i}$	= rotation from the i-th panel to the body reference frame
$\mathbf{a}_B^{w,q}$	= orientation of the q-th wheel spin axis in body axes
c_d	= diffuse reflectivity coefficient
\mathbf{C}_M	= adimensional aerodynamic momentum coefficient vector
\mathbf{C}_{Ma}	= dimensional aerodynamic momentum coefficient vector
c_p	= normal pressure coefficient
c_s	= specular reflectivity coefficient
c_τ	= shear stress coefficient
E_Q	= equation of time
f	= Earth's flattening coefficient
h	= altitude
\mathbf{H}_{tot}	= total angular momentum of the system
\mathbf{H}_s	= angular momentum of the satellite
\mathbf{H}_p	= angular momentum of the panels
\mathbf{H}_w	= angular momentum of the wheels
\mathbf{J}_s	= time-varying inertia matrix of the satellite
$\mathbf{J}_{p,i}$	= inertia matrix of the i-th panel
$\mathbf{J}_{w,q}$	= spin axis moment of inertia of the q-th wheel
K_n	= Knudsen number
LHA_\odot	= local hour angle
l_{ref}	= reference length
l_s	= panels support length
m	= satellite mass
M_\odot	= mean anomaly of the Sun
m_b	= residual dipole moment
M_j	= j-th triangular mesh element
m_m	= molecular mass of atmospheric constituents
M_{tot}	= total number of elements in the mesh
$\hat{\mathbf{n}}$	= outward normal unit vector
p	= i-th panel
P_N	= angular position of the panel (nominal minimum drag)
P_R	= angular position of the panel (non-nominal)

q_d	=	dynamic pressure
R	=	universal constant of gas
r_{\odot}	=	Sun's position vector
r_{CoM}	=	position vector of satellite CoM with regards to the geometric centre
r_e	=	Earth's equatorial radius
r_I	=	satellite inertial position vector
r_j	=	distance between the barycenter of the j-th element and the geometric centre of the satellite
r_{PO}	=	distance between the centre of mass and the centre of pressure
s	=	molecular speed ratio
S_j	=	surface of the j-th element
S_{ref}	=	reference surface
t_0	=	initial epoch in ephemeris seconds past J2000
T_a	=	aerodynamic torques vector
T_{alt}	=	temperature at altitude
T_d	=	disturbance torques vector
T_e	=	external torques vector
T_i	=	incident particles temperature
T_r	=	reflected particles temperature
t_s	=	sampling time
T_w	=	surface temperature
u_a	=	aerodynamic control signal
u_w	=	reaction wheel control signal
v_b	=	gas bulk velocity
v_I	=	satellite inertial velocity vector
v_{rel}	=	satellite velocity vector relatively to the flow
v_{rot}	=	atmospheric corotation velocity vector
v_t	=	atmospheric particle thermal speed
v_w	=	atmospheric winds velocity vector
w_{mb}	=	main bus width
w_Q	=	weighting coefficients for the state space
w_R	=	weighting coefficients for the control input
x	=	state space vector

x_e	=	error state space vector
$x_{pi}y_{pi}z_{pi}$	=	i-th panel reference frame
x_{ref}	=	reference state space vector
$X_B Y_B Z_B$	=	body reference frame
$Y_{B,m}, Z_{B,m}$	=	Y and Z body coordinates of the m-th mesh element vertex
Y_{CoM}, Z_{CoM}	=	Y and Z body coordinates of the CoM
α_k	=	angle of attack
α_n	=	normal thermal energy accommodation coefficient
α_T	=	thermal energy accommodation coefficient
β_k	=	angle of sideslip
γ_p	=	weighting coefficient
δ	=	angle of incidence of the flow (measured from the normal to the surface)
ϵ	=	obliquity of the ecliptic
ϑ_{max}	=	saturation angle of deflection of the panels
$\vartheta_{p,i}$	=	angle of deflection of the i-th panel
ϑ_{pl}	=	panels minimum angle of deflection (plant)
ϑ_s	=	panels minimum angle of deflection (algorithm)
λ_{E_\odot}	=	ecliptic longitude of the Sun
λ_{M_\odot}	=	mean longitude of the Sun
ν_M	=	mean anomaly
ρ	=	thermospheric density
σ_n, σ_t	=	normal/tangential momentum accommodation coefficient
$\hat{\tau}$	=	unit tangent vector
ϕ	=	roll angle
ϕ_{gd}	=	geodetic latitude
ϕ_l	=	reference longitude
φ	=	pitch angle
ψ	=	yaw angle
ω_B^I	=	inertially referenced body angular rates
$\omega_{p,i}$	=	angular velocity vector of the i-th panel relatively to the satellite bus
$\omega_{w,q}$	=	angular velocity of the q-th wheel about its spin axis
ω_\oplus	=	Earth's angular velocity vector

I. Introduction

THE majority of space missions in low Earth orbit (LEO) are characterised by operational altitudes spanning from 600 to 2000 km. The lower altitude range - extending below 600 km - is generally avoided for practical applications due to the numerous challenges that the enhanced disturbance environment poses to the platform design. Satellites travelling in these orbits experience increased magnetic dipole interactions, gravity gradient, aerodynamic torques, and similar effects due to solar radiation pressure present at higher altitude orbits. This is especially true in the very low Earth orbit range (VLEO), i.e. below 450 km, where the order of magnitude of the aerodynamic torques is the most significant disturbing contribution to the system dynamics. Despite the numerous obstacles, the advantages associated with the selection of lower altitudes are relevant, especially with regards to Earth observation [1, 2] and communication applications [3]. The possibility of improving performance for comparable payload specifications or, alternatively, to reduce missions costs for a given performance profile has recently sparked the interest of the scientific community, as evidenced by the increasing number of studies investigating operations in VLEO [4–7].

However, as the harshness of the environment increases, the requirements imposed on the attitude determination and control system (ADCS) become more stringent. Momentum-based devices, such as reaction wheels (RWs) and control momentum gyroscopes (CMGs), are efficient means to compensate for cyclical disturbances, perform smooth re-orientation manoeuvring, and counteract the secular external perturbations affecting the satellite's dynamics and kinematics. However, in an environment where aerodynamic disturbance dominates, momentum wheels may be susceptible to faster saturation with an obvious impact on the possibility to sustain operations. If on one hand VLEOs represent a challenge for mission design, on the other hand they offer the unique opportunity to investigate the application of novel control schemes that take advantage of the thermospheric environment rather than trying to fight against it. As the aerodynamic torques are the prevalent source of external disturbance, investigating whether their magnitude and direction could be modified in order to provide a low cost means for momentum unloading appears reasonable. The enhanced aerodynamic torques experienced by satellites at these altitudes can also be employed to implement hybrid active attitude control strategies. As many spacecraft are endowed with appendages extending from the bus, flat surfaces like solar panels can be used as aerodynamic actuators to support internal momentum devices while performing pointing control tasks. The combined employment of aerodynamic and conventional actuators may prove to be especially useful when actuator failure occurs [8], when size and volume restrictions are demanding, when at very low altitudes (<250 km) or during periods of intense solar activity the experienced aerodynamic torques may be too large for conventional actuators to handle the control task alone, or more generally when the requirement imposed on agility and accuracy are less onerous.

The greatest challenge, when implementing active aerodynamic attitude control, is addressing the uncertainties that characterise the problem formulation. The majority of studies propose to achieve aerodynamic attitude control by selecting the angles of rotation of allocated aerodynamic control actuators [4, 9–16]. A simple and quick way of

estimating the control torque is obtained by assuming small attitudes with regards to the incoming flow and limited ranges of deflection of the panels so that approximate linear laws can be used [4, 9–12, 16]. Alternative approaches see the implementation of an optimal control problem to find the time-varying position of the panels to minimise a desired cost function [14], or the use of truncated Fourier series [17] to obtain an estimation of the aerodynamic torques. In order to privilege the demonstration of the control concept, some studies assume in first approximation time-invariant aerodynamic coefficients and neglect the small contribution due to the aerodynamic lift to the computation of the aerodynamic torques [9, 10, 15]. For the computation of the aerodynamic coefficients, most investigations generally assume diffuse re-emission with complete [9] or incomplete [4, 11, 14] accommodation of the particles to the surface, or include some specular re-emission component by applying partial accommodation theory [12, 16]. Atmospheric density is modelled by means of exponential [12, 16], sinusoid [9], and atmospheric models [4, 11, 14]. Studies employing atmospheric models generally benefit from a more accurate description of other environmental parameters, such as the expected temperature at the selected altitude, atmospheric composition and molecular speed ratio, which are otherwise commonly neglected [12, 16, 17]. Inclusion of thermospheric winds in the determination of the direction of impingement of the particles is usually ignored, with some exceptions [4]. The applicability of aerodynamic control techniques have been evaluated against some of the uncertainties mentioned above in only a limited number of studies [11, 14, 15].

This paper has the purpose of: 1) providing a comprehensive background on the challenges affecting aerodynamic torque modelling in VLEO; 2) proposing an on-line algorithm for the determination of the control panels configuration that provides the closest match to a required input control signal; 3) testing the algorithm sensitivity to uncertainties and identifying critical conditions for operations for the case of some combined aerodynamic and RWs pointing manoeuvres. According to this, the paper is organised in the following way: section II discusses the sources of variability of the aerodynamic control authority in VLEO; section III provides a brief description of the principal features of the satellite geometry assumed; section IV defines the mathematical model for the satellite dynamics keeping into account the time-varying effects of the rotation of the appendages; section V is devoted to the design of the algorithm for selecting the angles of deflection of the aerodynamic actuators providing the desired control torque; validation under a limited set of assumptions and considering as many sources of uncertainty as possible, is addressed and discussed in section VI. Finally, in section VII, the robustness of the algorithm is demonstrated by means of a Monte Carlo analysis and potential limits of the controller are discussed to identify an optimal range of operations.

II. Aerodynamic control authority in VLEO

Accurate prediction of the control authority achievable in VLEO is hindered by the complex mechanisms involved in the generation of the aerodynamic torques. Because of this, works discussing means of exploitation of aerodynamic torques in VLEO generally rely on an apparatus of assumptions that are introduced with the scope of reducing the

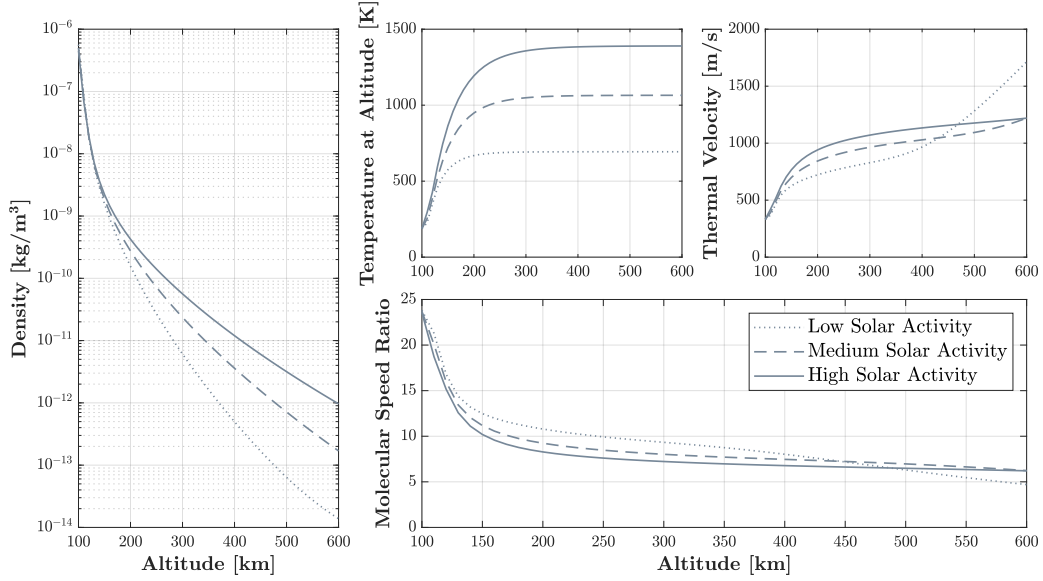


Fig. 1 Variation of environmental parameters with altitude and solar activity.

number of degrees of freedom involved. The parameters required to estimate the aerodynamic torques (\mathbf{T}_a) can be explicitly or implicitly inferred from their well-known mathematical formulation:

$$\mathbf{T}_a = \mathbf{r}_{PO} \times m \mathbf{a}_A = \frac{1}{2} \rho v_{rel}^2 S_{ref} \ell_{ref} \mathbf{C}_M \quad (1)$$

where \mathbf{r}_{PO} indicates the vector defining the distance between the CoP and the CoM, m is the satellite mass, \mathbf{a}_A is the aerodynamic acceleration vector, ρ is the atmospheric density, v_{rel} is the magnitude of the satellite velocity with regards to incoming flow, S_{ref} and ℓ_{ref} are the reference surface and length used to perform the computation and $\mathbf{C}_M = \{C_\phi, C_\varphi, C_\psi\}$ is the vector of the three aerodynamic momentum coefficients in roll (ϕ), pitch (φ) and yaw (ψ). As clearly stated by Eq. 1, alterations in the induced aerodynamic torques are expected with varying orbital/environmental conditions ($\frac{1}{2} \rho v_{rel}^2$) and platform characteristics ($S_{ref} \ell_{ref} \mathbf{C}_M$).

A. The role of the orbital and environmental conditions

The thermospheric environment mainly exerts its impact through the altitude-dependent variations of ρ and v_{rel} , the components of the dynamic pressure:

$$q_d = \frac{1}{2} \rho v_{rel}^2 \quad (2)$$

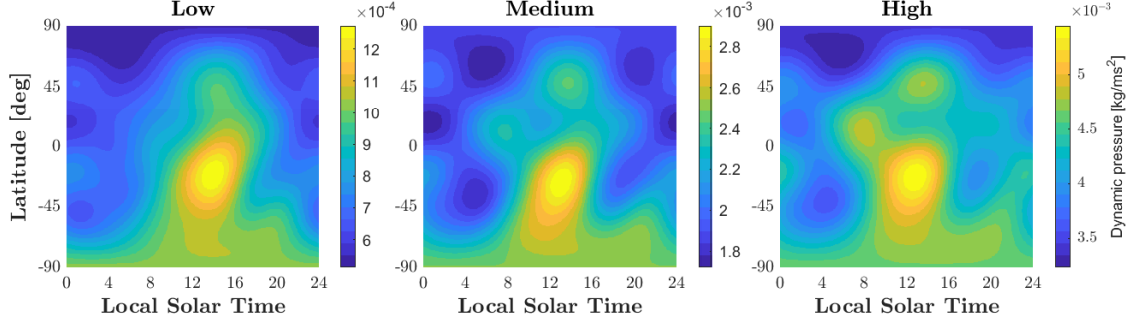


Fig. 2 Dynamic pressure variations with latitude, local solar time, and solar activity at 250 km.

Less significant variations are observed in the molecular speed ratio (s), that defines the relative order of magnitude of the gas bulk velocity (v_b) and the most probable thermal speed of the particles (v_t):

$$s = \frac{v_b}{v_t} = \frac{v_b}{\sqrt{\frac{2RT_{alt}}{m_m}}} \quad (3)$$

where $R = 8314 \text{ J kmol}^{-1} \text{ K}^{-1}$ is the universal constant of gas, m_m is the molecular mass of the atmospheric constituents and T_{alt} is the temperature at the altitude considered in K. The thermospheric flow has a drifting Maxwellian velocity distribution characterised by $v_t \ll v_b$. The effect of v_t is thus generally negligible and can be ignored, unless aerodynamic coefficients are computed for grazing angles of incidence. Although atmospheric density is mainly characterised by an exponential decay profile with altitude (Fig. 1, left), spatial and temporal fluctuations are observed in concomitance with alterations in the amount of thermal energy deposited in the lower thermosphere. The latter is subject to change with a number of physical processes, the most relevant being the 11-year cyclical variation of solar activity, the day-to-night, the seasonal-latitudinal, and the annual and semi-annual variations [18]. In Fig.1 the trends of the environmental parameters with altitude and solar activity for a reference longitude ($\phi_l = 0^\circ$) during low (1st Jan 2020), medium (1st Jan 2023), and high solar activity (1st Jan 2026) is shown. The NRLMSISE-00 model [19] and the solar and magnetic indices defined by ISO 1422:2013 [20] are used. As a consequence of the thermospheric expansion caused by the increased energy absorption, the mean molecular weight of the atmospheric constituents at a given altitude increases during periods of high solar activity and an overall increase in neutral density is observed (Fig. 1, left). The effect of the particle thermal velocity at higher altitudes become more relevant as the solar activity attenuates (Fig. 1, top right), so that variations of the molecular speed ratio are more noticeable for quiet atmospheric conditions at altitudes $> 400 \text{ km}$ (Fig. 1, bottom). Altitudes $< 150 \text{ km}$ see abrupt variations of the environmental parameters with height and consequently bigger uncertainties in the estimation of the aerodynamic torques. The aerodynamic drag induced in these orbits is however so high that operations cannot be sustained for a meaningful duration without compensation.

Modifications in temperature, gradients of pressure, kinematic viscosity and molecules-to-atoms ratio further affects

the dynamics of the upper atmosphere through the generation of atmospheric winds. As discussed in more detail in section V.B, the satellite inertial velocity at a certain altitude (v_I) and relative velocity with regards to the incoming flow (v_{rel}) do not generally coincide, as the velocity relative to the flow also takes into account the contributions due to atmospheric corotation (v_{rot}) and thermospheric winds (v_w). While satellite inertial velocity and atmospheric co-rotation can be derived with substantial accuracy, the same cannot be said about the thermospheric winds component. As a consequence, a precise knowledge of the satellite attitude with regards to the incoming flow is not currently achievable. However, since the order of magnitude of the satellite inertial velocity is predominant, for the sole purpose of defining the aerodynamic control authority expected in VLEO, $v_I \simeq v_{rel}$ can be reasonably assumed. This approximation was taken into account in Fig. 2, which shows the local variations of the dynamic pressure predicted by the NRLMSISE-00 atmospheric model [19] at 250 km for a range of latitudes, local solar times and solar conditions. Because of the Earth's rotation, the atmosphere warming is not homogeneous and a bulge, corresponding to a maximum in ρ , is clearly visible in all the three maps. Whilst the core appears to be centered at local solar time $\simeq 14-15$, its peripheral extension on both latitude and local solar time and its magnitude vary significantly according to solar cycle progression and the Sun's declination.

B. The role of the variables related to the platform design

Some control over the generated aerodynamic torques can be achieved through a proper selection of the satellite geometry and the materials employed for the external surfaces. In VLEO, despite the higher number density of constituents, the non-dimensional Knudsen number (K_n) is large enough so that $K_n \rightarrow \infty$ can be reasonably assumed. In these conditions, the flow is characterised by a high degree of rarefaction and it is generally referred to as a *free molecular flow* (FMF). The FMF regime is characterised by the predominance of surface-particles collisions over inter-particles collisions. As a consequence, the leading mechanism involved in the generation of the aerodynamic torques in VLEO is identifiable with the thermal energy and momentum exchange between the incident atmospheric particles and the external surfaces. A number of gas-surface interaction (GSI) models have been developed with the scope of providing a mathematical formulation for the aerodynamic coefficients and the exchange with the surfaces [21–27]. Reviews of some well-known GSI models in relation to the orbital aerodynamics problem are available [28, 29]. However, at present a simple GSI model capable of capturing different interaction scenario with accuracy is not available. Due to the high degree of contamination by atomic oxygen (AO) adsorption [30], common materials used on spacecraft typically show diffuse re-emission patterns corresponding to high energy and momentum exchange. However, gas-beam experimental results show that quasi-specular lobular re-emission patterns, characterised by reduced accommodation to the surface, are achievable when smooth and clean surfaces are employed [31]. Few studies showing interest towards a novel generation of aerodynamic materials resistant to AO adsorption are already present in literature [32, 33]. If their scattering characteristic can be demonstrated to be consistent over time, there might be an attractive possibility to employ

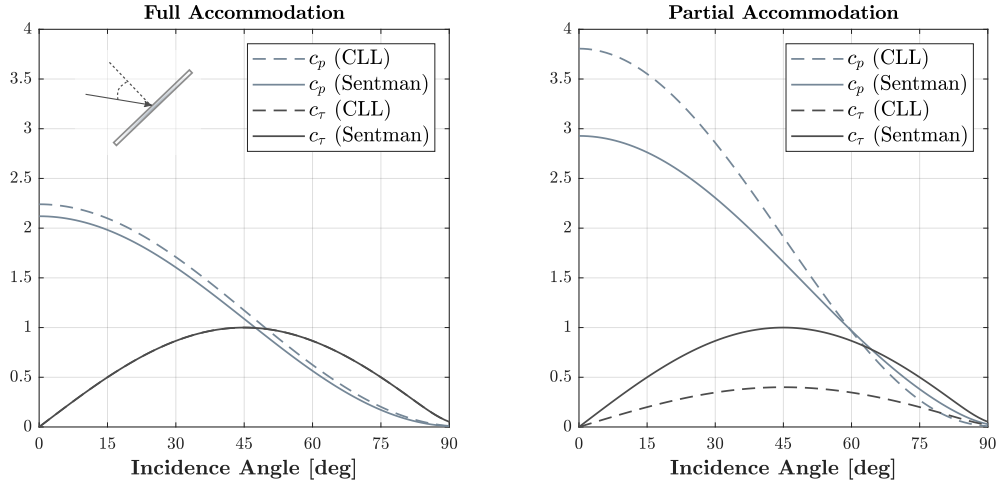


Fig. 3 Variation of c_p and c_τ on a flat plate with the re-emission characteristic (GSI model), the particles degree of accommodation, and the incident angle.

higher-performing aerodynamic materials for on-orbit applications. Fig. 3 compares the aerodynamic performance of a flat plate for varying re-emission profiles, incidence angles and incident particle accommodation. To perform this analysis, Sentman's model [21] was employed to model diffuse re-emission, while the Schaaf and Chambre analytical equations modified by Walker et al. [34] according to the Cercignani-Lampis-Lord (CLL) model assumptions were used to simulate the performance of quasi-specular materials. Uncertainties in the estimation of the aerodynamic coefficients is given by the normal pressure (c_p) and the shear stress (c_τ) coefficient components. Substantial qualitative and quantitative agreement between the models is observed when the incident particles attain complete accommodation with the surfaces (Fig. 3, left), as deviations mainly lie in the normal pressure component. Conversely, the predicted values of c_p and c_τ change significantly with the model and the re-emission mechanism assumed in the presence of partial accommodation (Fig. 3, right). Higher aerodynamic coefficients, and thus potentially higher aerodynamic control authority, is achievable for quasi-specular re-emissions and reduced particle accommodation. For intermediate scenarios, an imprecise knowledge of the particles accommodation to the surface translates to a source of uncertainty in aerodynamic modelling.

As revealed by Eq. 1 and by Fig. 3, the aerodynamic control capability is also susceptible to the geometric characteristics of the platform. For a given attitude with regards to the flow, the induced aerodynamic coefficients vary with the area exposed to the flow and with the angle at which the atmospheric particles impact the surfaces. Alterations in both characteristics are obtainable by moving or rotating some designated control actuators. The effect of external geometry alteration on the induced non dimensional aerodynamic coefficients is shown in Fig. 5, for a satellite with a cuboid bus and two aerodynamic panels located at the rear of the CoM (Fig. 4). Variation in the induced pitch and yaw torques can be easily achieved by introducing some asymmetries in the satellite external configuration so that corotation

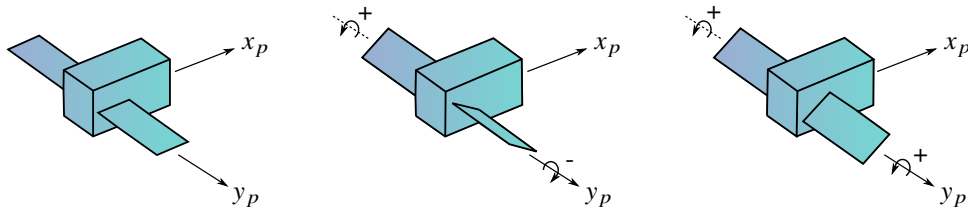


Fig. 4 Generic 2U CubeSat geometry with minimum drag (left), symmetrical counter-rotated (middle), and symmetrical co-rotated (right) configurations.

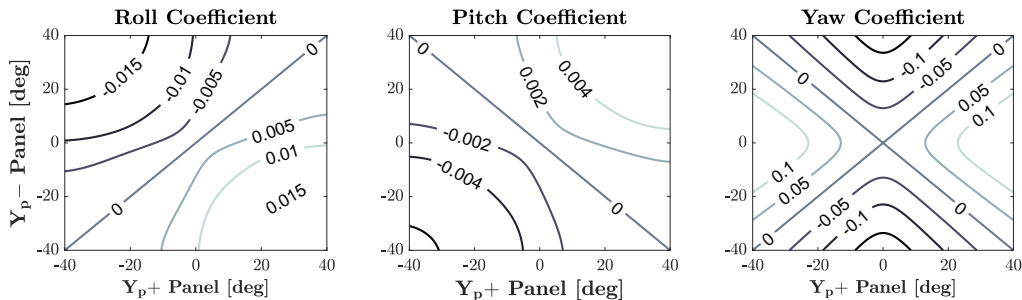


Fig. 5 Variation of the aerodynamic coefficients in roll, pitch and yaw with the relative angles of deflection of two aerodynamic panels extending along the side of a cuboid satellite.

of the panels can be commanded for this purpose (Fig. 5, middle and right). Conversely, variations in the roll coefficient require counter-rotation of the panels, with better results achievable when symmetrical configurations are selected (Fig. 5, left). For a given configuration of the actuators, variations in the induced aerodynamic coefficients are also expected to occur with attitude, as evidenced by the maps for the pitch and yaw coefficients of Fig. 6 that refer to the 2U satellite in its minimum drag configuration (Fig. 4, left), the total area of the panels, and the relative distance between the CoP and the CoM.

Due to the flow conditions, for a given surface exposed to the flow, discrepancies between the expected and the effectively induced aerodynamic torques may arise from panel shadowing: this phenomenon occurs when the satellite attitude with regards to the flow is such that ram surfaces shield some portions of the downstream surfaces, preventing their interaction with the atmospheric particles. If shadowing affects control panels, a reduced flow interaction translates to an inferior achievable control authority. This effect is especially important when concave geometries in non-equatorial orbits are considered and the magnitude of thermospheric winds is relevant. In general, a convex design with long panels largely prevents surface shielding and multiple particles interactions from occurring. Under these circumstances, this phenomenon eventually involves just a very limited portion of the exposed surfaces.

The introduction of geometric considerations in VLEO is fundamental not only to increase the aerodynamic control authority, but also to minimise the induced aerodynamic drag. Because of its dissipative nature, it represents the primary drawback affecting applications in this altitude range. The use of movable control surfaces to perform attitude control

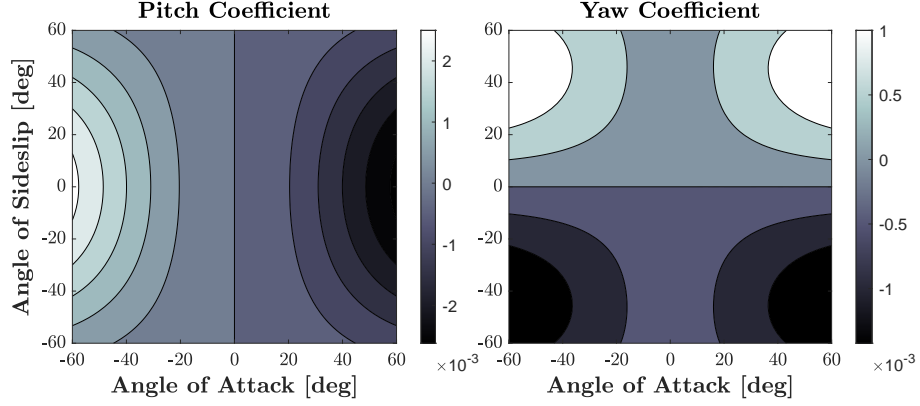


Fig. 6 Variation of the aerodynamic coefficients in pitch (left) and yaw (right) with attitude.

has an impact on the induced aerodynamic drag as a consequence of the generally increased projected area exposed, during manoeuvring, to the flow. Some shaping criteria, however, can be employed especially with regards to the satellite main body [35, 36]: while the panel configuration can be modified so that aerodynamic forces and torques can be usefully employed, the aerodynamic contribution due to the satellite main body represents a source of attitude and orbital disturbance for which minimisation is desirable.

III. Satellite geometry and aerodynamic design

The feathered geometry of SOAR [37] is selected as reference for the problem formulation and the validation of the results. The essential geometric characteristics of this satellite are shown in Fig. 7: SOAR is a 3U CubeSat characterised by four rotating panels mounted at rear of the satellite main body. Enhanced control authority in three-axes is achieved by setting the incidence angle of each panel with regards to the incoming flow independently: co-rotated and counter-rotated configurations of the vertical and horizontal panels can thus be achieved by rotating the selected appendages about their longitudinal axes (Fig. 7, right). Four reference frames are accordingly defined ($x_{p_i}, y_{p_i}, z_{p_i}$ for $i = 1, \dots, 4$) to describe the relative motion of each panel with regards to the moving satellite body reference frame $X_B Y_B Z_B$, which is assumed to be centered at the satellite composite CoM. Their orientation in the satellite nominal low-drag configuration is shown in Fig. 7. The origin of each panel reference frame is located at the centre of mass of the corresponding panel, which is assumed perfectly symmetric about its rotational axis and uniform in its mass distribution. The $X_B Y_B Z_B$ reference frame and the panels reference frames are aligned when the rotation angles of the four panels is set to zero, i.e. when the panels are in the nominal low drag configuration. For any other configuration, the orientation of each panel reference frame with regards to $X_B Y_B Z_B$ can be described by the associated direction cosine matrix. Positive and negative rotations of the aerodynamic surfaces are defined according the $X_B Y_B Z_B$ reference frame description following the right hand rule and they are consistent among the aerodynamic surfaces employed (Fig. 7, right).

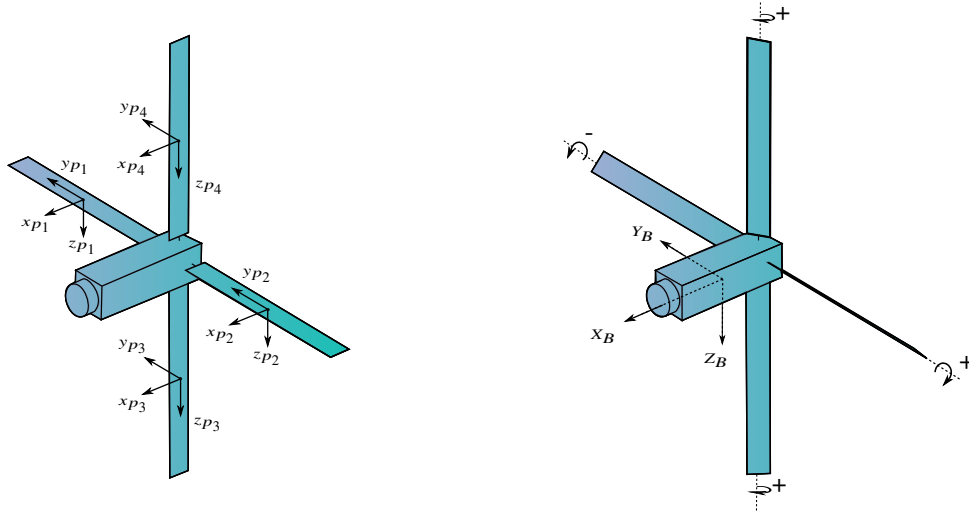


Fig. 7 SOAR's geometry for two representative configurations. Left: nominal low-drag configuration. Right: arbitrary panels configuration.

IV. Satellite dynamics with rotating appendages

When rotating aerodynamic actuators are employed for control purposes, the satellite dynamics about the center of mass is not only affected by the presence of the internal momentum devices (if present) but also by the rotational dynamics of these appendages. According to the principle of conservation of the angular momentum, an equivalence can be established between the inertially referenced rate of change of the angular momentum of a system about its centre of mass ($\dot{\mathbf{H}}_{tot}^I$) and the external torques acting on it (\mathbf{T}_e). Applying Euler's momentum formulation:

$$\dot{\mathbf{H}}_{tot}^I = \dot{\mathbf{H}}_{tot}^B + \boldsymbol{\omega}_B^I \times \mathbf{H}_{tot}^B \quad (4)$$

so that:

$$\dot{\mathbf{H}}_{tot}^B = \mathbf{T}_e - \boldsymbol{\omega}_B^I \times \mathbf{H}_{tot}^B \quad (5)$$

In Eqs. 4 and 5, \mathbf{T}_e generally includes the contribution due to aerodynamic torques (\mathbf{T}_a), disturbance torques (\mathbf{T}_d) and the control torques provided by the actuators, \mathbf{H}_{tot}^B is the total angular momentum in body axes, and $\boldsymbol{\omega}_B^I$ are the inertially referenced body angular rates. For the system considered in this paper, \mathbf{H}_{tot}^B is given by the sum of the angular momentum of the total satellite system (\mathbf{H}_s^B), the angular momentum of each rotating surface about its center of mass (\mathbf{H}_p^B) and the angular momentum of the RWs about their axis of rotation (\mathbf{H}_w^B), all represented in the satellite body frame:

$$\mathbf{H}_{tot}^B = \mathbf{H}_s^B + \mathbf{H}_p^B + \mathbf{H}_w^B = \mathbf{J}_s \boldsymbol{\omega}_B^I + \sum_{i=1}^{n_p} A_B^{p,i} \mathbf{J}_{p,i} \boldsymbol{\omega}_{p,i} + \sum_{q=1}^{n_w} \mathbf{J}_{w,q} \left(\mathbf{a}_B^{w,q} \cdot \boldsymbol{\omega}_B^I + \boldsymbol{\omega}_{w,q} \right) \mathbf{a}_B^{w,q} \quad (6)$$

where \mathbf{J}_s , \mathbf{J}_p and \mathbf{J}_w are respectively the inertia tensors of the total satellite, the panels, and the RWs, ω_p and ω_w indicate the angular rate of the panels and of the wheels about their spin axis, $A_B^{p,i}$ is the rotation matrix from the i -th appendage to the body reference frame, and $\mathbf{a}_B^{w,q}$ is the vector that defines the orientation of the q -th wheel in body axes. Computing the first time derivative of Eq. 6 relatively to the body reference frame, it is possible to get:

$$\dot{\mathbf{H}}_{tot}^B = \mathbf{J}_s \dot{\omega}_B^I + \dot{\mathbf{J}}_s \omega_B^I + \sum_{i=1}^{n_p} A_B^{p,i} \mathbf{J}_{p,i} (\dot{\omega}_{p,i})_B + \sum_{i=1}^{n_p} A_B^{p,i} (\dot{\mathbf{J}}_{p,i})_B \omega_{p,i} + \sum_{q=1}^{n_w} \mathbf{J}_{w,q} (\mathbf{a}_B^{w,q} \cdot \dot{\omega}_B^I + \dot{\omega}_{w,q}) \mathbf{a}_B^{w,q} \quad (7)$$

Assuming that the time variation of the total satellite inertia matrix is only due to the rotation of the aerodynamic surfaces with regards to the satellite main body [38]:

$$\dot{\mathbf{J}}_s = \sum_{i=1}^{n_p} A_B^{p,i} (\dot{\mathbf{J}}_{p,i})_B A_{p,i}^B \quad (8)$$

where $A_{p,i}^B = A_B^{p,iT}$. According to this, Eq. 7 can be re-arranged in the following way:

$$\dot{\mathbf{H}}_{tot}^B = \mathbf{J}_s \dot{\omega}_B^I + \dot{\mathbf{J}}_s \left(\omega_B^I + \sum_{i=1}^{n_p} A_B^{p,i} \omega_{p,i} \right) + \sum_{i=1}^{n_p} A_B^{p,i} \mathbf{J}_{p,i} (\dot{\omega}_{p,i})_B + \sum_{q=1}^{n_w} \mathbf{J}_{w,q} (\mathbf{a}_B^{w,q} \cdot \dot{\omega}_B^I + \dot{\omega}_{w,q}) \mathbf{a}_B^{w,q} \quad (9)$$

Recognising that:

$$\dot{\mathbf{H}}_w^B = \sum_{q=1}^{n_w} \mathbf{J}_{w,q} (\mathbf{a}_B^{w,q} \cdot \dot{\omega}_B^I + \dot{\omega}_{w,q}) \mathbf{a}_B^{w,q} \quad (10)$$

and substituting Eq. 6, 9 and 10 in Eq. 5, it is possible to get:

$$\dot{\omega}_B^I = \mathbf{J}_s^{-1} \left[\mathbf{T}_d + \mathbf{T}_a - \dot{\mathbf{J}}_s \left(\omega_B^I + \sum_{i=1}^{n_p} A_B^{p,i} \omega_{p,i} \right) - \sum_{i=1}^{n_p} A_B^{p,i} \mathbf{J}_{p,i} \dot{\omega}_{p,i} - \omega_B^I \times \left(\mathbf{J}_s \omega_B^I + \sum_{i=1}^{n_p} A_B^{p,i} \mathbf{J}_{p,i} \omega_{p,i} + \mathbf{H}_w^B \right) - \dot{\mathbf{H}}_w^B \right] \quad (11)$$

Removing the contributions due to the appendages rotations in Eq. 11, the well known formulation of the rigid-body rotational equation for a satellite equipped with reaction wheels is obtained. For the specific case of the geometry considered, the matrix $A_{p,i}^B$, which describes the transformation to be applied from the body axes to the selected panels reference frame, assumes the form $A_{p,1/2}^B$ for the horizontal panels and $A_{p,3/4}^B$ for the vertical ones:

$$A_{p,1/2}^B = \begin{bmatrix} \cos(\vartheta_{p,1/2}) & 0 & -\sin(\vartheta_{p,1/2}) \\ 0 & 1 & 0 \\ \sin(\vartheta_{p,1/2}) & 0 & \cos(\vartheta_{p,1/2}) \end{bmatrix} \quad A_{p,3/4}^B = \begin{bmatrix} \cos(\vartheta_{p,3/4}) & \sin(\vartheta_{p,3/4}) & 0 \\ -\sin(\vartheta_{p,3/4}) & \cos(\vartheta_{p,3/4}) & 0 \\ 0 & 0 & 1 \end{bmatrix} \quad (12)$$

where $\vartheta_{p,1/2}$ and $\vartheta_{p,3/4}$ indicate the angle of rotation of the horizontal and vertical panels, respectively. More significant perturbations are introduced in the system when both the vertical and horizontal panels are symmetrically corotated and

high angular velocities $\omega_{p,i}$ of the panels are used. Disturbances cancel for the selection of symmetrical counter-rotated configurations of pairs of opposing panels.

V. On-line algorithm for active aerodynamic attitude control

In order to perform aerodynamic active attitude control, the commanded torque computed by a selected control law ($\mathbf{u}_a \approx \mathbf{T}_a$) at a given time step t_k needs to be provided in input to an algorithm that accordingly selects the corresponding angles of deflection of the aerodynamic actuators. The decision process of the algorithm proposed in this study - here referred to with the acronym PCA (panel configuration algorithm) - is based on the on-line computation of the expected aerodynamic torques for the current satellite attitude. A qualitative and general representation of the flow of operations that, from the control signal produced by a generic control law, leads to the selection of the angles of deflection of the panels is provided in Fig. 8. A detailed description is given in the following.

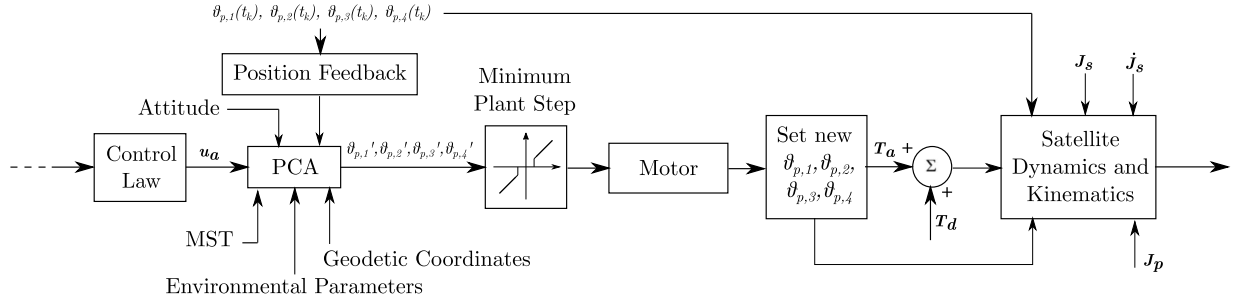


Fig. 8 General representation of the framework for the implementation of the PCA algorithm.

A. Atmospheric density modelling

In order to take into account the discrepancies observed with altitude, solar activity, geographic location and diurnal variations, the approach used in this study relies on the linear interpolation of some reference values of ρ contained in a lookup table. For given solar weather conditions, these values are computed by using the NRLMSISE-00 atmospheric model [19] for a limited range of variation of VLEO altitudes, latitudes and local solar times. To limit the size of the lookup table within acceptable dimensions, the solar activity is fixed and selected according to the expected solar weather conditions at a reference epoch.

Linear interpolation of the atmospheric density values in the lookup table requires the estimation of the geodetic latitude (ϕ_{gd}), altitude (h) and local solar time at the time step $t_k = t_0 + kt_s$, where t_0 is the initial epoch expressed in ephemeris seconds past J2000 and t_s is the sampling time. The geodetic latitude and the altitude are computed from the ITRF93 referenced satellite position vector according to the algorithm proposed in [39], which was modified to use the Earth's equatorial radius ($r_e = 6378.2064$ km) and flattening coefficient ($f = 1/294.9787$) of the Clark66 spheroid. Since the accuracy requirement imposed on the calculation of the local solar time is moderate, an approximate but quick

implementation is preferred. If the small differences between UT1 and barycentrical dynamical time are neglected, the corresponding number of Julian centuries referred to a given t_k are approximately equivalent ($T_{UT1} \approx T_{TDB}$). The Sun's mean longitude (λ_{M_\odot}), mean anomaly (M_\odot) and ecliptic longitude (λ_{E_\odot}) can be accordingly computed as [40, pp. 277–281]:

$$\lambda_{M_\odot} = 280.460^\circ + 36000.771 T_{UT1} \quad (13a)$$

$$M_\odot \simeq 357.5291092^\circ + 35999.05034 T_{UT1} \quad (13b)$$

$$\lambda_{E_\odot} = \lambda_{M_\odot} + 1.914666471^\circ \sin(M_\odot) + 0.019994643 \sin(2M_\odot) \quad (13c)$$

Once the obliquity of the ecliptic (ϵ) has been determined:

$$\epsilon \simeq 23.439291^\circ - 0.0130042 T_{UT1} \quad (14)$$

the Sun's position vector (\mathbf{r}_\odot) can be derived using [40, pp. 277–281]:

$$r_\odot = 1.000140612 - 0.016708617 \cos(M_\odot) - 0.000139589 \cos(2M_\odot) \quad (15a)$$

$$\mathbf{r}_\odot = [r_\odot \cos(\lambda_{E_\odot}), r_\odot \cos(\epsilon) \sin(\lambda_{E_\odot}), r_\odot \sin(\epsilon) \sin(\lambda_{E_\odot})]^T \text{ AU.} \quad (15b)$$

After converting 15b to the proper unit of measurement, the satellite inertial position vector (\mathbf{r}_I) and the Sun's position vector (\mathbf{r}_\odot) are used to compute the local hour angle [40, p. 1002]:

$$LHA_\odot = \frac{180^\circ}{\pi} \left[\frac{r_{\odot,x} r_{I,y} - r_{\odot,y} r_{I,x}}{|r_{\odot,x} r_{I,y} - r_{\odot,y} r_{I,x}|} \arccos \left(\frac{r_{\odot,x} r_{I,x} + r_{\odot,y} r_{I,y}}{\sqrt{r_{\odot,x}^2 + r_{\odot,y}^2} \sqrt{r_{I,x}^2 + r_{I,y}^2}} \right) \right] \quad (16)$$

The mean local solar time (MST) is finally computed as the difference between the local apparent solar time ($LAST$) and the equation of time (E_Q), where [40, p. 178]:

$$LAST = LHA_\odot + 180^\circ \quad (17a)$$

$$E_Q = -1.914666471^\circ \sin(M_\odot) - 0.019994643 \sin(2M_\odot) + 2.466 \sin(2\lambda_{E_\odot}) - 0.0053 \sin(4\lambda_{E_\odot}) \quad (17b)$$

B. Relative velocity estimation

As discussed in section II, the induced aerodynamic coefficients have a dependence on the satellite attitude with regards to the incoming flow. This can be deduced from the expression of \mathbf{v}_{rel} in the J2000 reference frame:

$$\mathbf{v}_{rel} = \mathbf{v}_I + \mathbf{v}_{rot} + \mathbf{v}_w = \mathbf{v}_I + (\boldsymbol{\omega}_{\oplus} \times \mathbf{r}_I) + \mathbf{v}_w \quad (18)$$

In order to simulate an imperfect knowledge of the incoming flow direction (Section II.A), the contribution due to \mathbf{v}_w in Eq. 18 is not considered by the PCA. The vector \mathbf{v}_{rel} derived accordingly is then used to determine, at each time step t_k , the rotation matrix from body-axes to wind-axes (A_F^B) and the corresponding angle of attack (α_k) and sideslip (β_k):

$$\alpha_k = \arcsin\left(-A_F^B(3, 1)\right) \quad \text{and} \quad \beta_k = \arcsin\left(A_F^B(1, 2)\right) \quad (19)$$

C. Selecting the configuration of the panels

Once q_d and the satellite attitude with regards to the impinging flow ($A_B^F = A_F^{BT}$) have been determined, the PCA selects the panel configuration providing the closest match between the induced aerodynamic torques \mathbf{T}_a (Eq. 1) and the input control signal $\mathbf{u}_a(t_k)$. In order to compute the dimensional aerodynamic coefficients $\mathbf{C}_{M_d} = S_{ref} \ell_{ref} \mathbf{C}_M$ in Eq. 1, a quick online computation technique is utilised. This algorithm is based on ADBSat [11, 41], a panel method for aerodynamic performance computation developed at the University of Manchester. The original ADBSat software, envisaged as an off-line tool to determine the aerodynamic characteristics of a geometry immersed in FMF, was modified to provide online computation of the dimensional aerodynamic coefficients for multiple control panel permutations and varying re-emission characteristics under the computational speed requirement imposed by the stability of a discrete-time control loop with a sampling time $t_s = 1s$.

The PCA firstly reads the cartesian coordinates of a simplified triangular mesh that describes the geometry of the satellite in its nominal low drag configuration $P_N = [0^\circ, 0^\circ, 0^\circ, 0^\circ]$. The total number of elements in the mesh (M_{tot}) is limited not only to reduce the computational effort, but also to contain the size of the input data used by the algorithm. A geometric criteria, based on the characteristic dimensions of the satellite, is then used to identify the triangular surface elements in the mesh belonging to the p_1, p_2, p_3 and p_4 panels from those that belong to the satellite main body:

$$M_j \in p_1 \Leftrightarrow \forall Y_{B,m} \in M_j, Y_{B,m} \geq (w_{mb}/2 - Y_{CoM} + l_s) \quad (20a)$$

$$M_j \in p_2 \Leftrightarrow \forall Y_{B,m} \in M_j, Y_{B,m} \leq -(w_{mb}/2 + Y_{CoM} + l_s) \quad (20b)$$

$$M_j \in p_3 \Leftrightarrow \forall Z_{B,m} \in M_j, Z_{B,m} \geq (w_{mb}/2 - Z_{CoM} + l_s) \quad (20c)$$

$$M_j \in p_4 \Leftrightarrow \forall Z_{B,m} \in M_j, Z_{B,m} \leq -(w_{mb}/2 + Z_{CoM} + l_s) \quad (20d)$$

where M_j is the j -th element of the triangular mesh inspected, $Y_{B,m}$ and $Z_{B,m}$ with $m = 1, 2, 3$ are the body-referenced coordinates of the m -th vertex that constitutes the M_j triangular mesh element considered, Y_{CoM} and Z_{CoM} are the body-referenced coordinates of the CoM measured from the geometric centre of the satellite, w_{mb} is the width of the satellite main body and l_s is the length of the support by which each panel is connected to the main body. To simulate the aerodynamic performance of different materials, a thermal accommodation coefficient ($\alpha_{T,j}$), describing the extent to which the particles achieve thermal accommodation with the surface, is associated to the elements identified in the mesh:

$$\alpha_{T,j} = \frac{T_i - T_{r,j}}{T_i - T_{w,j}} \quad (21)$$

where T_i and $T_{r,j}$ are respectively the kinetic temperatures of the incident and re-emitted particles and $T_{w,j} = T_w = 300 \text{ K} = \text{const}$ is the averages surface temperature. Variations of the surface temperature, albeit present, are not modelled, as the associated variations of the thermal accommodation coefficient are generally difficult to address in a physically meaningful way. Future improvements in orbital aerodynamic science may enable to establish a better correlation of this latter with the environment, the spacecraft thermal model, and the material selection. Once the main body and the control surfaces have been identified, the algorithm computes the aerodynamic coefficients for a range of possible satellite configurations by rotating each panel about its longitudinal axis. Since no particular restriction is imposed on the panel movement, the number of possible permutations can be high, especially if small angular steps (ϑ_s) are considered. In order to reduce the computational effort, only a limited number of possible configurations is selected by the PCA. For each panel, a vector ap_i containing three angular positions is defined according to the following definition:

$$ap_i = \left[\lfloor \vartheta_{p,i_k} / \vartheta_s \rfloor \vartheta_s - \vartheta_s, \lfloor \vartheta_{p,i_k} / \vartheta_s \rfloor \vartheta_s, \lfloor \vartheta_{p,i_k} / \vartheta_s \rfloor \vartheta_s + \vartheta_s \right]^T \quad \text{for } i = 1, \dots, 4 \quad (22)$$

where ϑ_{p,i_k} is the estimated angle of deflection of the i -th panel at the time step t_k , ϑ_s is the reference rotation angle of the panels used to perform the computation of the aerodynamic coefficients, and $\lfloor x \rfloor$ indicates the floor function for $x = \vartheta_{p,i_k} / \vartheta_s$. The selection of the angles of deflection for each panel is subjected to the definition of a saturation limit for the actuators ($\pm \vartheta_{max}$), so that:

$$ap_i = \{ap_{i1}, ap_{i2}, ap_{i3} : -\vartheta_{max} \leq ap_{i1}, ap_{i2}, ap_{i3} \leq \vartheta_{max}\} \quad (23)$$

A rectangular grid (P_R) containing the combinations of the angular positions specified in ap_1 , ap_2 , ap_3 and ap_4 is then

created, so that:

$$P_R = \begin{bmatrix} ap_{11} & ap_{21} & ap_{31} & ap_{41} \\ ap_{12} & ap_{21} & ap_{31} & ap_{41} \\ \vdots & \vdots & \vdots & \vdots \\ ap_{12} & ap_{23} & ap_{33} & ap_{43} \\ ap_{13} & ap_{23} & ap_{33} & ap_{43} \end{bmatrix} \quad (24)$$

Each row in the P_R matrix defines a configuration of the aerodynamic panels. For any of these, the PCA reads the angles of deflection associated with the panels and rotates the coordinates of the corresponding elements in the mesh by applying the rotation matrices described in Eq. 12. The PCA then proceeds to the computation of the dimensional aerodynamic coefficients in Eq. 1. For the n-th configuration considered, these are given by:

$$\mathbf{C}_{M_d}^{(n)} = \mathbf{C}_M^{(n)} S_{ref} \ell_{ref} = \sum_{j=1}^{M_{tot}} (\mathbf{r}_j - \mathbf{r}_{CoM}) \times \left(c_{\tau_j}^{(n)} \hat{\boldsymbol{\tau}}_j^{(n)} - c_{p_j}^{(n)} \hat{\mathbf{n}}_j^{(n)} \right) S_j \quad (25)$$

where \mathbf{r}_j is the vector that describes the distance between the barycenter of the j-th element in the mesh and the geometric centre of the satellite, \mathbf{r}_{CoM} is the position vector of the satellite CoM measured from the satellite geometric centre, $c_{\tau_j}^{(n)}$ and $c_{p_j}^{(n)}$ are respectively the aerodynamic shear stress and normal pressure coefficients, $\hat{\mathbf{n}}_j^{(n)}$ is the outward unit normal vector, S_j is the area and $\hat{\boldsymbol{\tau}}_j^{(n)}$ is the unit tangent vector of the j-th element considered in the mesh.

The definition of the aerodynamic coefficients $c_{p_j}^{(n)}$ and $c_{\tau_j}^{(n)}$ is not necessarily unique. As discussed in section II.B different analytical expressions are given according to the assumed re-emission mechanism of the particles and the GSI model employed to describe it. For the application discussed in this paper, these will be chosen considering the limited performance achievable by common materials. In these regards, Sentman's model [21] is widely used to describe diffuse particle re-emissions from contaminated surfaces and will therefore be adopted:

$$c_{p_j}^{(n)} = \frac{\cos(\delta_j^{(n)})}{\sqrt{\pi}s} e^{-s^2 \cos^2(\delta_j^{(n)})} + \left(\frac{1}{2s^2} + \cos^2(\delta_j^{(n)}) \right) \left[1 + \operatorname{erf}(s \cos(\delta_j^{(n)})) \right] + \frac{1}{2} \sqrt{\frac{2}{3}} \left[1 + \alpha_{T,j} \left(\frac{T_w}{T_i} - 1 \right) \right] \left\{ \sqrt{\pi} \cos(\delta_j^{(n)}) \left[1 + \operatorname{erf}(s \cos(\delta_j^{(n)})) \right] + \frac{1}{s} e^{-s^2 \cos^2(\delta_j^{(n)})} \right\} \quad (26a)$$

$$c_{\tau_j}^{(n)} = \frac{\sin(\delta_j^{(n)})}{\sqrt{\pi}s} \left\{ e^{-s^2 \cos^2(\delta_j^{(n)})} + \sqrt{\pi}s \cos(\delta_j^{(n)}) \left[1 + \operatorname{erf}(s \cos(\delta_j^{(n)})) \right] \right\} \quad (26b)$$

where s is the molecular speed ratio (see Eq. 3), T_w is the wall temperature, $\alpha_{T,j}$ is the thermal accommodation coefficient defined in Eq. 21, $T_i = \frac{2}{3}s^2 T_{alt}$ is the kinetic temperature of the incident flow expressed as a function of the thermospheric temperature at the specified altitude (T_{alt}), and $\delta_j^{(n)}$ is the angle between the incident flow and the normal to each surface element in the mesh for the n-th configuration considered. Approximated values of s and T_{alt} are

obtained by linear interpolation of some averaged reference values provided by the NRLMSISE-00 model [19] for the space weather conditions at the epoch selected (see Tab. 1). To reduce the number of computations to be performed, the

Table 1 Averaged reference values of s and T_{alt} .

Altitude [km]	Molecular speed ratio	Temperature at altitude [K]
200	10.6657	669.3270
210	10.4548	676.1180
220	10.2676	681.0724
230	10.1002	684.7046
240	9.9499	687.3797
250	9.8145	689.3585
260	9.6921	690.8283
270	9.5806	691.9243
280	9.4781	692.7448
290	9.3826	693.3612

dimensional aerodynamic coefficients in Eq. 25 are computed separately for the mesh elements belonging to the main body ($C_{M_{a,B}}$) and the mesh elements belonging to the control panels rotated at the angles specified in P_R ($C_{M_{a,P}}^{(n)}$). The contribution due to the satellite main body is determined by the attitude of the satellite with regards to the flow and it is therefore the same for all the configurations considered. For the n -th configuration, the expected aerodynamic control torque is then computed as:

$$\mathbf{T}_a^{(n)} = q_d \left(C_{M_{a,B}} + C_{M_{a,P}}^{(n)} \right) \quad (27)$$

The angular position of the fins selected by the PCA is the one for which the induced aerodynamic torques best match the commanded control torques while minimising as much as possible the induced aerodynamic drag. The desired configuration is the one that produces the minimum Euclidean distance (d_{L_2}) between the vectors \mathbf{T}_{ref} and \mathbf{T}_{exp} :

$$\left[\vartheta_{p,1}^{(n)}, \vartheta_{p,2}^{(n)}, \vartheta_{p,3}^{(n)}, \vartheta_{p,4}^{(n)} \right] \Leftrightarrow d_{L_2}^{(n)}(\mathbf{T}_{ref}, \mathbf{T}_{exp}^{(n)}) = \sqrt{\sum_{ii=1}^l \left(T_{ref,ii} - T_{exp,ii}^{(n)} \right)^2} \equiv \min [d_{L_2}(\mathbf{T}_{ref}, \mathbf{T}_{exp})] \quad (28)$$

with $\mathbf{T}_{ref} = [\mathbf{u}_{a,k}, P_N]$ and $\mathbf{T}_{exp}^{(n)} = [\mathbf{T}_a^{(n)}, \gamma_p |P_{R_{n,*}}|]$, where P_N is the vector of the panels angles in the nominal low drag configuration expressed in radians, $|P_{R_{n,*}}|$ is the absolute value in radians of the angles of deflection of the four panels as they are defined for each configuration in P_R and γ_p is a weighting coefficient. If multiple configurations providing the same torque are identified, the one that requires the least movement of the control surfaces is selected in order to reduce the disturbance introduced in the total system dynamics.

VI. Validation of the PCA algorithm and discussion

This section discusses the capability of the PCA algorithm described in section V to select, at each time step t_k , a configuration of the panels providing the required torque $\mathbf{u}_a(t_k)$ received in input. For this purpose, the aerodynamic control torque induced about the desired control axes by the selected angles of deflection of the actuators is compared

- 2) Thermospheric winds are neglected in the decision process of the PCA (section V.B), but these are included in the determination of the angle of attack and sideslip when determining the actual aerodynamic torque provided by the panels. The HWM93 model [44] is used for this purpose.
- 3) Differently from the PCA, the simulation environment assumes partial particle accommodation. Due to the low altitude orbit considered and the performance of typical materials a realistic value of $\alpha_T = 0.95$ is employed.
- 4) The four panels are constrained to rotate with an angular speed of $\omega_{p,i} = 0.8^\circ/\text{s}$ and they are subject to a saturation limit of $\vartheta_{max} = \pm 60^\circ$. The angular step used to perform the computation in the PCA is $\vartheta_s = \pm 4^\circ$. A minimum angular step for the plant ($\vartheta_{pl} = \vartheta_s$) is also introduced, so that if the commanded $\vartheta_{p,i} < \vartheta_{pl}$, the i -th panel would be kept in the nominal configuration.
- 5) The performance of off-the-shelf components available for platforms similar to the one considered is reproduced. The approach followed is based on GomSpace's characterisation of the UKF attitude determination capability of SOAR. Attitude knowledge error is modeled as gaussian noise corresponding to the filtered 2σ value obtainable with the Epson M-G370 gyro suite and a three-axis magnetometer at 200 km during periods of eclipse (0.42°) and Sun (0.43°). Analogously, errors in the determination of the panels angular positions are modelled as gaussian noise according to the performance of the AM4096 - 12 bit angular magnetic encoder, by using as a conservative estimation position errors of $\pm 0.2^\circ$. Inertial angular body rates are recovered from gyro measurements as in Ref. [45, pp. 266-270]: white gyro noise is modelled as a function of the angle random walk expected for the M-G370 gyro suite. A $\pm 10\%$ uncertainty is introduced on the angular steps of the panels, according to the performance expected for a Faulhaber two-phase stepper motor.
- 6) The impact of the rotating appendages on the satellite dynamics is included in the simulated system behaviour. The main geometric characteristics of SOAR are summarised in Tab. 2, where the coordinates of the CoM are measured from the satellite geometric centre according to the body axes convention. Due to its convex geometry and the extension of the control surfaces with regards to the main body dimensions, panel shadowing can be reasonably neglected.

Table 2 SOAR's geometric features. Symbols ℓ , w and t respectively indicate length, width and thickness.

Main bus [m]	Panels [m]	Panel support [m]	CoM location [m]	Inertia tensor [kg m ²]
$\ell = 0.3660$	$\ell = 0.3660$	$\ell = 0.007$	$r_{CoM} = \begin{bmatrix} -22.01e^{-3} \\ -0.999e^{-3} \\ 0.77e^{-3} \end{bmatrix}$	$J_s = \begin{bmatrix} 0.0543 & 1.00e^{-5} & -7.79e^{-6} \\ 1.00e^{-5} & 0.0627 & -2.21e^{-6} \\ -7.79e^{-6} & -2.21e^{-6} & 0.0627 \end{bmatrix}$
$w = 0.1$	$w = 0.060$	-		
-	$t = 0.001$	-		

Fig. 10 shows the values of the environmental parameters computed using the approximate decision process of the PCA algorithm and the more accurate NRLMSISE-00 atmospheric model [19] over the duration of the pointing manoeuvre shown in Fig. 12. Any discrepancy between the values expected by the PCA algorithm and the actual environmental conditions represents a source of uncertainty against which the algorithm must show robustness. As expected, the estimation of the molecular speed ratio and the temperature at the current altitude performed by the

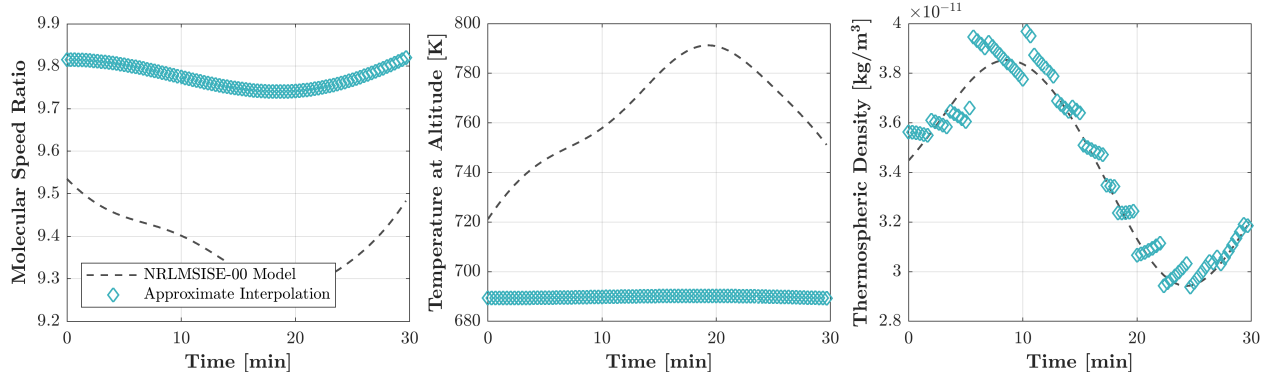


Fig. 10 Values of the environmental parameters as they are computed by: 1) the simple linear interpolation performed by the PCA and 2) the NRLMSISE-00 atmospheric model [19].

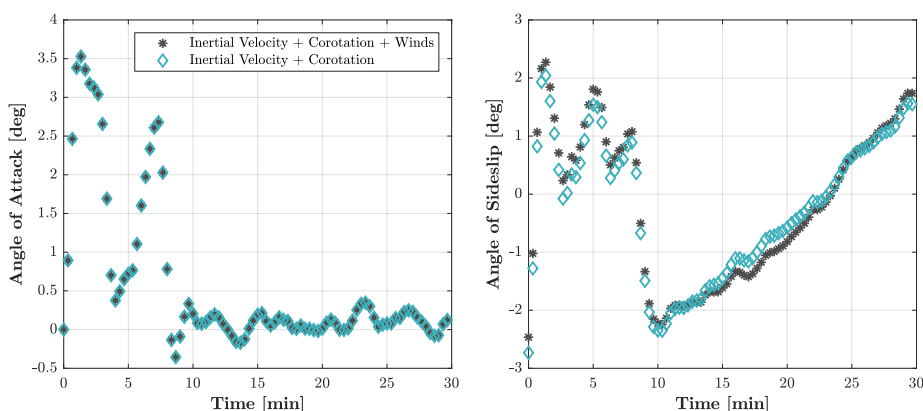


Fig. 11 Attitude estimation considering: 1) the inertial velocity and the atmospheric corotation vectors (PCA algorithm); 2) the inertial velocity, the atmospheric corotation, and the horizontal winds vector (induced aerodynamic output).

algorithm is fairly constant. The quick and simplified logic designed is not capable of capturing short-scale temporal and spatial variations, accounted for the NRLMSISE-00 model. As evidenced by the right plot in Fig. 10, discrepancies in the estimation of ρ may cause the algorithm to partially underestimate or overestimate the control authority effectively achievable. Differences with the values predicted by the atmospheric model are due to the fact that a very limited range of reference latitudes and local solar time values are considered for the interpolation of the approximate density. Moreover, Fig. 11 shows that when horizontal winds are included in the computation of the aerodynamic torque induced by the panels, discrepancies with the PCA algorithm are observed in the computation of the angle of sideslip. Inclusions of vertical winds, which are here neglected, are expected to introduce some small uncertainties also in the determination of the angle of attack.

Given these premises, Fig. 12 shows the behaviour of the PCA algorithm while performing an aerodynamic attitude control manoeuvre to stabilise the motion about the roll axis from an initial offset of $\phi = 20^\circ$, and an initial body

angular rate of $0.5^\circ/\text{s}$. Aerodynamic control authority is maximised by limiting the decision process of the PCA to panels counter rotated configurations. The control signal results from setting alignment with the Local Vertical Local Horizontal reference frame [46, pp. 36–37] as the desired final state. The aerodynamic control torque induced by the configuration of the panels selected by the PCA at each time step (blue solid line in Fig. 12, left) is compared against the corresponding command torque computed by the quaternion feedback PID controller (orange solid line in Fig. 12, left). Despite the uncertainties described above, the trend observed in the command torque is qualitatively reproduced by the aerodynamic torque induced by the panels. The quantitative differences observable at the beginning of the manoeuvre are likely to derive from the requirement imposed on the speed of rotation of the panels.

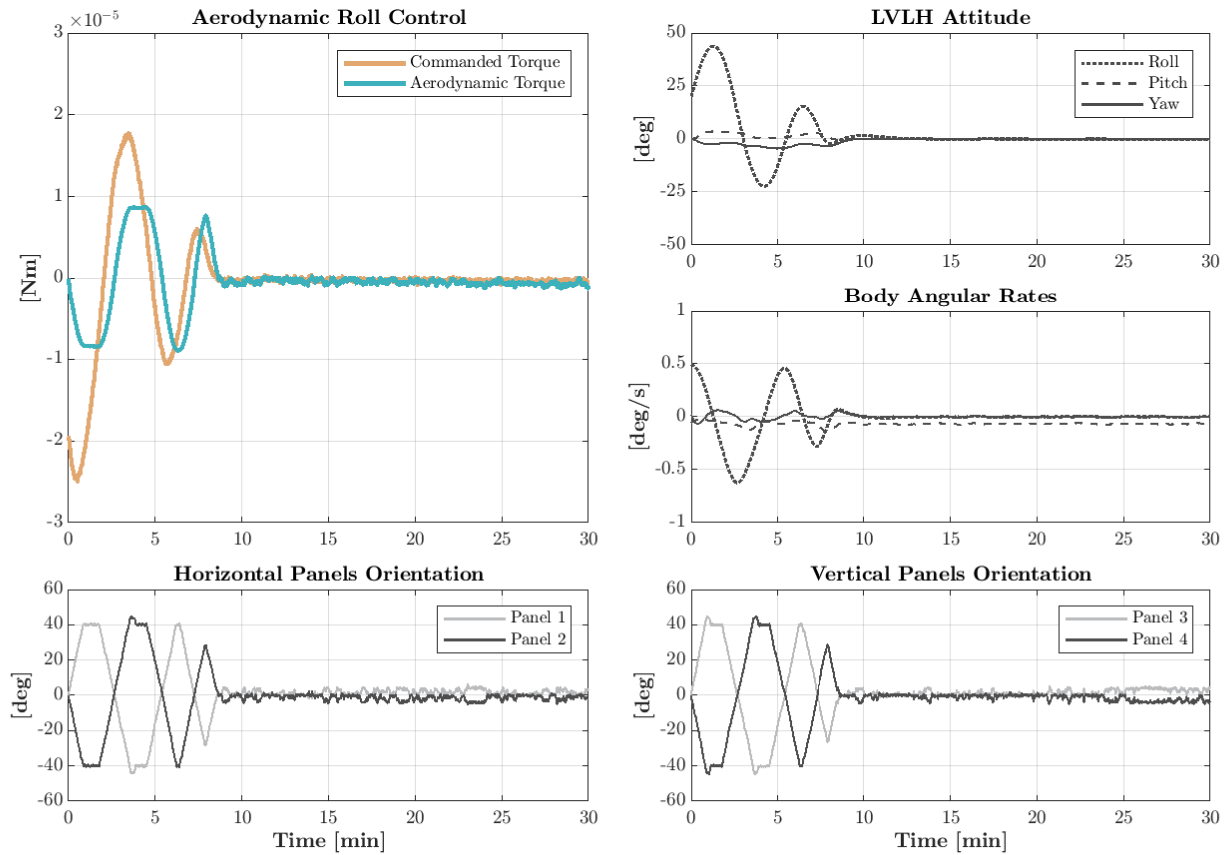


Fig. 12 Validation of the PCA algorithm for the case of a roll aerodynamic attitude control manoeuvre.

VII. Robustness analysis

A Monte Carlo simulation was performed to assess the sensitivity of the algorithm in the presence of uncertain modelling and to identify under which circumstances the simple aerodynamic controller proposed may fail. The parameters utilised in the simulation are shown in Tab. 3. The implementation of the PCA algorithm, the system considered, and the lookup table used to predict density are unvaried and coincide with the ones discussed in the

previous sections. A combined manoeuvre for which aerodynamic panels are commanded to control the pitch and yaw dynamics and RWs are used to stabilise the roll motion, is assumed (Fig. 9). For the aerodynamic coefficient computation, the PCA assumes that the CoM is located at its nominal position (see Tab. 3) for all the case studies considered: the effect of ignoring the CoM "true" position can thus be accordingly addressed in the results discussion. The quaternion feedback PID [43] gains are determined by using an optimal linear quadratic regulator approach [47]. For all the cases considered these are derived by always selecting the same weighting coefficients for the state space ($w_Q = [1, 1, 1]^T$) and the control input ($w_R = [1e^{11}, 1e^{12}, 1e^{12}]^T$) matrices, assumed diagonal. The range of values for each variable (see Tab. 3) has been defined with the specific purpose of probing the failure conditions for the controller. For practical applications orbital parameters such as RAAN and orbit inclination are typically known with considerably higher confidence. Similarly, PID gains can be tuned for altitude uncertainties that are smaller than those considered. CoM knowledge accuracy is generally in the order of millimeters/centimeters. A wider range of altitudes, however, offers the chance to assess to what extent simple control laws, such as a quaternion feedback PID, can be considered robust when used in combination with the proposed algorithm to implement aerodynamic control. The question appears relevant, since PIDs are in practice the industrial standard for most space applications. Analogously, reduced CoM-CoP distances may provide information on some design criteria that may be relevant especially during quiet solar cycle conditions. Since off-nominal conditions are expected to have an impact especially on the capability of damping the platform residual rates, a challenging scenario was considered. Aerodynamic control was initiated with an initial offset of $\varphi = -20^\circ$ in pitch and $\psi = 20^\circ$ in yaw and angular body rates of $-0.5^\circ/\text{s}$ and $0.5^\circ/\text{s}$ about the pitch and yaw axes, respectively. The target state imposed is alignment with the LVLH reference frame [46, pp. 36–37]. For each instance considered, the manoeuvre was considered failed if saturation of at least one wheel in the assembly occurred before the satellite attitude was stabilised. Vice versa, the manoeuvre was assumed to be successfully achieved if the satellite attitude was coarsely stabilised with steady state errors below 3° for more than 30 s without incurring in RWs saturation. In the presence of larger steady state errors but no RWs saturation, the manoeuvre was considered achieved but with degraded performance. Results obtained by random selection of the independent variables for 200

Table 3 Ranges of variation of the independent variables used to perform the Monte Carlo analysis.

Variable	Nominal Value	Range
Epoch	2020 Apr 15 04:50:00	[2020 Jan 1, 2021 Jan 1]
α_T	0.95	[0.8, 1]
RAAN [deg]	0	[0, 360]
Inclination [deg]	51.6	[0, 90]
Altitude [km]	250	[230, 270]
CoM location [m]	-0.0220086	[-0.061, 0.061]

samples are shown in Fig. 13 and Fig. 14. In Fig. 13, orange dots indicate failed samples, whilst dots with a color gradient ranging from white to dark blue identify successful samples. Darker colors are associated to successful samples

with longer settling times and thus inferior performance. The outcome of the simulation is displayed in such a manner that covariance of the independent variables can be discussed. As expected, the majority of failures occur when the aerodynamic control authority experienced is substantially lower than that predicted by the controller. This condition

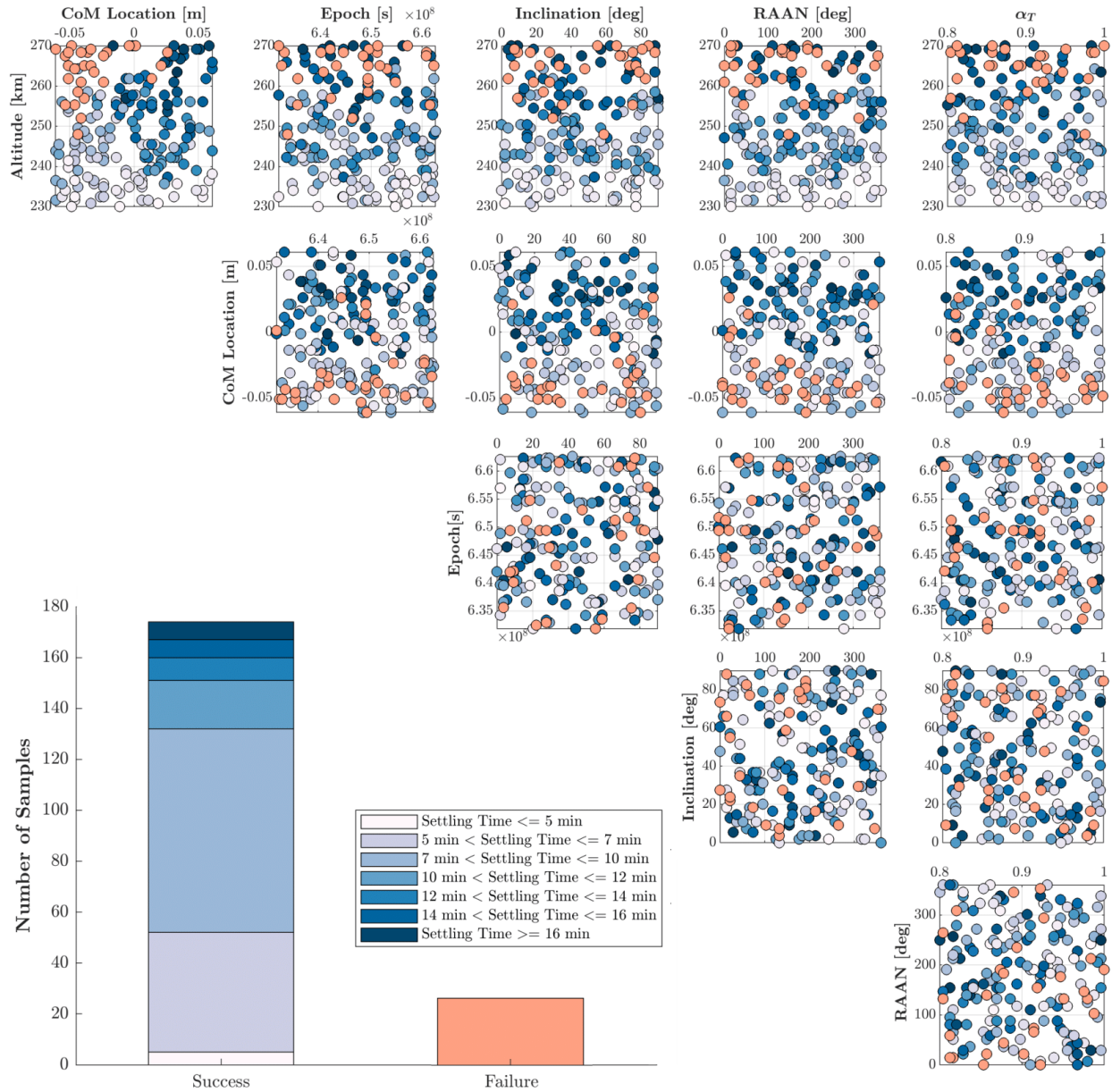


Fig. 13 Top right: covariance plots of the independent variables values selected by the random process of the Monte Carlo simulation. Bottom left: bar plots of the failed (orange) and successful (blue scale) samples considered.

occurs when two conditions are verified: 1) operations are conducted at increased altitudes, and 2) a platform with a reduced offset between the CoM and the CoP is utilised (i.e. the CoM is located behind the geometric centre of the bus). The inability to damp the residual body rates does not only depend on the reduced aerodynamic control authority on

itself, but also by the fact that the utilised set of gains were selected for more favourable control conditions (nominal parameters value in Tab. 3). When the aerodynamic authority reduces, if the gains are too small, energy damping is not fast enough and saturation of the reaction wheels quickly occurs. This suggests a conclusion that is somewhat expected: to achieve comparable performance in different conditions using a simple PID, gains scheduling is required. However, the selection of more favourable conditions for at least one parameter between altitude and the CoM location seems to be enough to assure the robustness of the algorithm under the uncertainties considered. Lower altitudes and/or longer CoM-CoP distances result in increased aerodynamic torques and thus better performance. In this regard, it is interesting to notice how moving the CoM forward of the geometric centre of the main bus may efficiently compensate for density reduction at higher altitudes. The relevant uncertainties affecting the algorithm decision process translates to longer settling times but does not result in the failure of the manoeuvre. For the CubeSat satellite class, however, any solution for shifting forward the CoM or to move back the CoP can be only utilised after orbit insertion: launch requirements impose the CoM to be located within 2 cm from the geometric centre. Since the diurnal bulge is the most relevant feature for density variations on a horizontal plane, the effect of coupling with seasonal uncertainties is generally small, as evidenced by the altitude and CoM plots against epoch. Orbit inclination, RAAN and α_T overall seem to have a smaller impact on the sensitivity of the controller. Results, however, are expected to vary according to solar activity conditions considered. For intense solar irradiance, the behaviour of the algorithm at higher altitudes and reduced CoM-CoP distances is expected to improve due to a general increase of atmospheric density over the VLEO range (see Fig. 1). On the other hand, inclination is expected to have a more substantial role especially at higher latitudes, where thermospheric winds may reach velocities of 400 m/s [48]. In general, even better results are expected to be observed for less demanding control manoeuvres. Overall results seem to suggest that during quiet solar activity is recommended to perform operations below 250 km, where atmospheric density is high enough for manoeuvring. The capability to attain the target attitude for 87% of the samples, despite the large width of variation of the independent variables considered, attests the robustness of the controller.

Some of the considerations that have been made here are confirmed by the time histories of the pitch and yaw dynamics displayed in Fig. 14. In this case, color codes are used to discuss the impact of the altitude on accuracy, overshoot, and settling time of the manoeuvre. As expected, generally worse performance is associated with manoeuvring at higher altitudes. Reduced overshoot, smaller settling times, and improved accuracy are instead observed especially for samples at 230-240 km. Some deviations from this general trend are however observed, as a result of the selection of the other independent variables in the problem. To an extent, it is possible that higher steady state errors observed in some cases may result from utilising a set of gains that was not optimal for the orbital conditions. In the worst case displayed, however, the satellite attitude is constrained between $\pm 5^\circ$ from the desired final target. Under the current technological level (available performance of materials) and low solar activity conditions, only coarse aerodynamic pointing can be expected. However, in the near future potential improvements may be achieved with the utilisation of

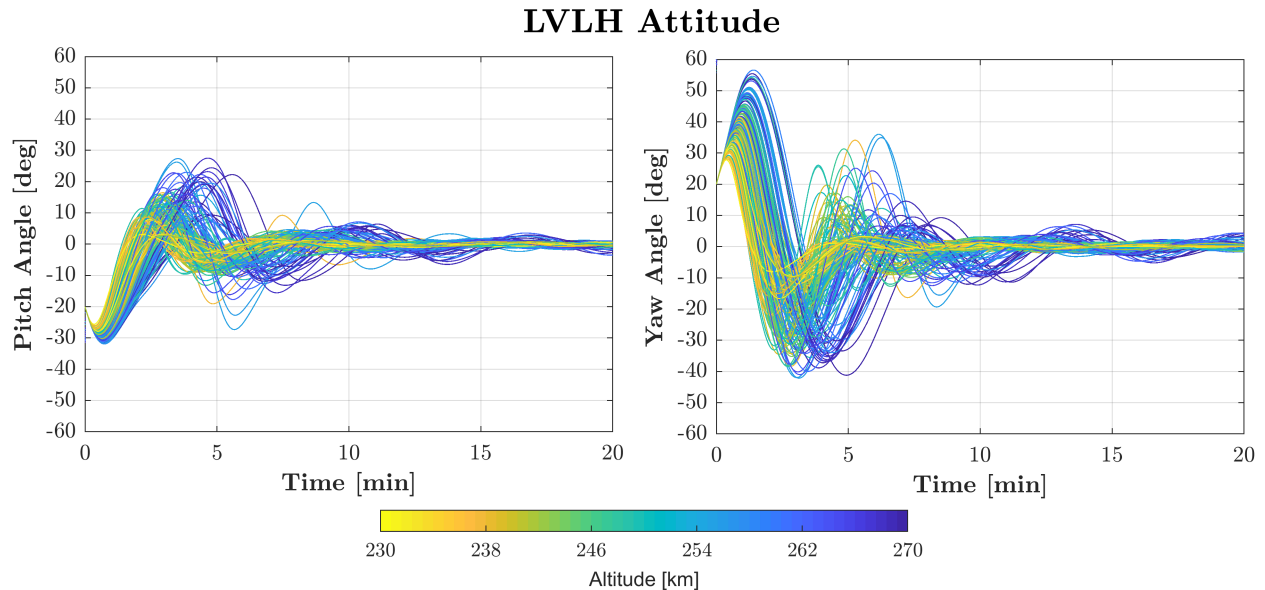


Fig. 14 Time histories of the pitch and yaw angles for each sample cases considered in the Monte Carlo analysis. Color coding is attributed according to the Monte Carlo simulation altitudes.

quasi-specularly reflecting materials, improved hardware and software specifications, and with an increased confidence in estimating density and thermospheric winds.

VIII. Conclusions

The algorithm proposed to actuate four independent control surfaces to achieve active aerodynamic control was validated by assuming representative case studies for combined aerodynamic and reaction wheels attitude pointing. The results of the Monte Carlo analysis performed show that, even when a simple quaternion feedback PID is used to determine the input control signal, coarse pointing is achieved and the algorithm ensures robustness against uncertainties, inaccurate environmental modelling, and attitude hardware limitations. Critical conditions for the utilisation of aerodynamic control during quiet solar activity are presented when the control authority significantly reduces (high VLEO altitudes with small CoM-CoP offsets) and, at the same time, the set of gains selected for the quaternion feedback PID control law is not appropriate to assure fast damping. Overall, operations in VLEO may significantly benefit from an advantageous use of the aerodynamic environment to perform attitude control tasks.

Acknowledgements

The authors of this paper are grateful to the members of the DISCOVERER project and to Dr David Mostaza Prieto for their suggestions, and for sharing their research experience with them. This project has received funding from the European Union's Horizon 2020 research and innovation programme under grant agreement No 737183. This publication reflects only the view of the authors. The European Commission is not responsible for any use that may be

made of the information it contains.

References

- [1] Crisp, N. H., Roberts, P. C., Livadiotti, S., Oiko, V. T., Edmondson, S., Haigh, S. J., Huyton, C., Sinpetru, L. A., Smith, K. L., Worrall, S. D., Becedas, J., Domínguez, R. M., González, D., Hanessian, V., Mølgaard, A., Nielsen, J., Bisgaard, M., Chan, Y. A., Fasoulas, S., Herdrich, G. H., Romano, F., Traub, C., García-Almiñana, D., Rodríguez-Donaire, S., Sureda, M., Kataria, D., Outlaw, R., Belkouchi, B., Conte, A., Perez, J. S., Villain, R., Heißerer, B., and Schwalber, A., “The benefits of very low earth orbit for earth observation missions,” *Progress in Aerospace Sciences*, Vol. 117, No. December 2019, 2020. <https://doi.org/10.1016/j.paerosci.2020.100619>.
- [2] Virgili-Llop, J., Roberts, P. C. E., Hao, Z., Ramio Tomas, L., and Beauplet, V., “Very Low Earth Orbit mission concepts for Earth Observation. Benefits and challenges,” *Reinventing Space Conference 2014*, London, 2014, pp. 1 – 18.
- [3] Gavish, B., and Kalvenes, J., “The impact of satellite altitude on the performance of LEOS based communication systems,” *Wireless Networks*, Vol. 4, No. 2, 1998, pp. 119–213. <https://doi.org/10.1023/A:1019151905814>.
- [4] Cañas Muñoz, V., Gonzalez, D., Becedas, J., Domínguez, R. M., Roberts, P. C., Crisp, N. H., Oiko, V. T., Edmondson, S., Worrall, S. D., Haigh, S., Smith, K., Lyons, R. E., Livadiotti, S., Huyton, C., Sinpetru, L. A., Rodriguez-Donaire, S., Garcia-Almiñana, D., Nieto, M., Muñoz, C., Sureda, M., Kataria, D., Herdrich, G. H., Romano, F., Binder, T., Boxberger, A., Fasoulas, S., Traub, C., Outlaw, R., Hanessian, V., Morsbøl, J., Villain, R., Perez, J. S., Conte, A., Belkouchi, B., Schwalber, A., and Heisserer, B., “Attitude control for satellites flying in VLEO using aerodynamic surfaces,” *JBIS - Journal of the British Interplanetary Society*, Vol. 73, No. 3, 2020, pp. 103–112. URL <https://www.jbis.org.uk/paper/2020.73.103>.
- [5] Virgili Llop, J., Polat, H. C., and Romano, M., “Using shifting masses to reject aerodynamic perturbations and to maintain a stable attitude in very low Earth orbit,” *Advances in the Astronautical Sciences*, Vol. 158, 2016, pp. 2129–2148. URL <http://hdl.handle.net/10945/50863>.
- [6] Fujita, K., and Noda, A., “Aerodynamics of Satellites on a Super Low Earth Orbit,” *AIP Conference Proceedings*, Vol. 1084, 2008, pp. 772–777. <https://doi.org/10.1063/1.3076580>.
- [7] Romano, F., Chan, Y. A., Herdrich, G., Traub, C., Fasoulas, S., Roberts, P. C. E., Smith, K., Edmondson, S., Haigh, S., Crisp, N. H., Oiko, V. T. A., Worrall, S. D., Livadiotti, S., Huyton, C., Sinpetru, L. A., Straker, A., Becedas, J., Domínguez, R. M., González, D., Cañas, V., Sullioti-Linner, V., Hanessian, V., Mølgaard, A., Nielsen, J., Bisgaard, M., Garcia-Almiñana, D., Rodriguez-Donaire, S., Sureda, M., Kataria, D., Outlaw, R., Villain, R., Perez, J. S., Conte, A., Belkouchi, B., Schwalber, A., and Heißerer, B., “RF Helicon-based Inductive Plasma Thruster (IPT) Design for an Atmosphere-Breathing Electric Propulsion system (ABEP),” *Acta Astronautica*, Vol. 176, No. July, 2020, pp. 476–483. <https://doi.org/10.1016/j.actaastro.2020.07.008>.
- [8] Horri, N. M., and Palmer, P., “Practical implementation of attitude-control algorithms for an underactuated satellite,” *Journal of Guidance, Control, and Dynamics*, Vol. 35, No. 1, 2012, pp. 40–50. <https://doi.org/10.2514/1.54075>.

- [9] Burns, T. F., and Flashner, H., “Adaptive control applied to momentum unloading using the low earth orbital environment,” *Journal of Guidance, Control, and Dynamics*, Vol. 15, No. 2, 1992, pp. 325–333. <https://doi.org/10.2514/3.20840>.
- [10] Wang, X., Yao, Y., Guo, J., Liu, K., and Guo, Y., “Attitude control and momentum management of space station via weighted-state H_∞ method,” *Proceedings of the 33rd Chinese Control Conference, CCC 2014*, 2014, pp. 1001–1006. <https://doi.org/10.1109/ChiCC.2014.6896764>.
- [11] Mostaza Prieto, D., “Characterisation and Applications of Aerodynamic Torques on Satellites,” Ph.D. thesis, University of Manchester, 2017.
- [12] Gargasz, M. L., “Optimal Spacecraft Attitude Control Using Aerodynamic Torques,” Ph.D. thesis, Air Force Institute of Technology, 2007.
- [13] Virgili Llop, J., Roberts, P. C. E., and Hao, Z., “Aerodynamic attitude and orbit control capabilities of the Δ DSAT cubesat,” *Advances in the Astronautical Sciences*, Vol. 151, No. February, 2014, pp. 321–332.
- [14] Mostaza Prieto, D., and Roberts, P. C. E., “Perigee Attitude Maneuvers of Geostationary Satellites During Electric Orbit Raising,” *Journal of Guidance, Control, and Dynamics*, Vol. 40, No. 8, 2017, pp. 1978–1989. <https://doi.org/10.2514/1.G002370>.
- [15] Pande, K. C., and Venkatachalam, R., “On optimal aerodynamic attitude control of spacecraft,” *Acta Astronautica*, Vol. 6, No. 11, 1979, pp. 1351–1359. [https://doi.org/10.1016/0094-5765\(79\)90127-9](https://doi.org/10.1016/0094-5765(79)90127-9).
- [16] Auret, J., and Steyn, W. H., “Design of an aerodynamic attitude control system for a CubeSat,” *62nd International Astronautical Congress 2011, IAC 2011*, Vol. 11, No. January 2011, 2011, pp. 9009–9017.
- [17] Johnson, C. D., and Skelton, R. E., “Optimal desaturation of momentum exchange control systems,” *AIAA Journal*, Vol. 9, No. 1, 1971, pp. 12–21. <https://doi.org/10.1002/hep.23123>.
- [18] Emmert, J. T., “Thermospheric mass density: A review,” *Advances in Space Research*, Vol. 56, No. 5, 2015, pp. 773–824. <https://doi.org/10.1016/j.asr.2015.05.038>, URL <http://dx.doi.org/10.1016/j.asr.2015.05.038>.
- [19] Picone, J. M., Hedin, A. E., Drob, D. P., and Aikin, A. C., “NRLMSISE-00 empirical model of the atmosphere: Statistical comparisons and scientific issues,” *Journal of Geophysical Research: Space Physics*, Vol. 107, No. A12, 2002, pp. 0–16. <https://doi.org/10.1029/2002JA009430>.
- [20] International Organization for Standardization ISO, “Space environment (natural and artificial) - Earth upper atmosphere (ISO/DIS 14222),” 2013, p. 47. URL <http://www.spacewx.com/Docs/ISO{ }DIS{ }14222{ }E.pdf>.
- [21] Sentman, L. H., “Free molecule flow theory and its application to the determination of aerodynamic forces,” Tech. rep., Lockheed Aircraft Corporation, Sunnyvale, California, 1961. <https://doi.org/10.21236/ad0265409>.
- [22] Moe, K., and Moe, M. M., “Gas-surface interactions and satellite drag coefficients,” *Planetary and Space Science*, Vol. 53, No. 8, 2005, pp. 793–801. <https://doi.org/10.1016/j.pss.2005.03.005>.

- [23] Schamberg, R., “A new analytic representation of surface interaction with hypothermal free molecular flow with application to neutral-particle drag estimates of satellites,” Tech. rep., RAND, Research Memorandum, 1959.
- [24] Cook, G. E., “Satellite Drag Coefficients,” Tech. rep., Defense Documentation Center for Scientific and Technical Information, Cameron Station Alexandria, Virginia, 1965. <https://doi.org/10.1002/nav.3800080206>.
- [25] Schaaf, S. A., and Chambre, P. L., *Flow of Rarefied Gases*, Princeton university Press, 1958. URL <https://www.jstor.org/stable/j.cttm32248.4>.
- [26] Maxwell, J. C., *The Scientific Papers of James Clerk Maxwell*, Vol. II, Dover Publications, New York, 1890. <https://doi.org/10.1017/CBO9780511710377>.
- [27] Cercignani, C., and Lampis, M., “Kinetic models for gas-surface interactions,” *Transport Theory and Statistical Physics*, Vol. 1, No. 2, 1971, pp. 101–114. <https://doi.org/10.1080/00411457108231440>.
- [28] Mostaza Prieto, D., Graziano, B. P., and Roberts, P. C. E., “Spacecraft drag modelling,” *Progress in Aerospace Sciences*, Vol. 64, 2014, pp. 56–65. <https://doi.org/10.1016/j.paerosci.2013.09.001>.
- [29] Livadiotti, S., Crisp, N. H., Roberts, P. C. E., Worrall, S. D., Oiko, V. T. A., Edmondson, S., Haigh, S. J., Huyton, C., Smith, K. L., Sinpetru, L. A., Holmes, B. E. A., Becedas, J., Domínguez, R. M., Cañas, V., Christensen, S., Mølgaard, A., Nielsen, J., Bisgaard, M., Chan, Y., Herdrich, G. H., Romano, F., Fasoulas, S., Traub, C., Garcia-Almiñana, D., Rodriguez-Donaire, S., Sureda, M., Kataria, D., Belkouchi, B., Conte, A., Perez, J. S., Villain, R., and Outlaw, R., “A review of gas-surface interaction models for orbital aerodynamics applications,” *Progress in Aerospace Sciences*, Vol. 119, No. June, 2020, p. 100675. <https://doi.org/10.1016/j.paerosci.2020.100675>.
- [30] Banks, B. A., Miller, S. K., and de Groh, K. K., “Low Earth Orbital Atomic Oxygen Interactions With Materials,” , 2004. <https://doi.org/10.1557/PROC-851-NN8.1>, URL <http://hdl.handle.net/2060/20040087142>.
- [31] Goodman, F. O., “Review of the theory of the scattering of gas atoms by solid surfaces,” *Surface Science*, Vol. 26, No. 1, 1971, pp. 327–362. [https://doi.org/10.1016/0039-6028\(71\)90135-X](https://doi.org/10.1016/0039-6028(71)90135-X).
- [32] Murray, V. J., Pilinski, M. D., Smoll, E. J., Qian, M., Minton, T. K., Madzunkov, S. M., and Darrach, M. R., “Gas-Surface Scattering Dynamics Applied to Concentration of Gases for Mass Spectrometry in Tenuous Atmospheres,” *Journal of Physical Chemistry C*, Vol. 121, No. 14, 2017, pp. 7903–7922. <https://doi.org/10.1021/acs.jpcc.7b00456>.
- [33] Crisp, N. H., Macario-Rojas, A., Roberts, P. C. E., Edmondson, S., Haigh, S. J., Holmes, B. E. A., Livadiotti, S., Oiko, V. T. A., Smith, K. L., Sinpetru, L. A., Becedas, J., Domínguez, R. M., Sullioti-Linner, V., Christensen, S., Kauffman Jensen, T., Nielsen, J., Bisgaard, M., Chan, Y., Herdrich, G. H., Romano, F., Fasoulas, S., Traub, C., Garcia-Almiñana, D., Garcia-Berenguer, M., Rodriguez-Donaire, S., Sureda, M., Kataria, D., Belkouchi, B., Conte, A., Seminari, S., and Villain, R., “Investigation of Novel Drag-Reducing and Atomic Oxygen Resistant Materials in Very Low Earth Orbit using SOAR (Satellite for Orbital Aerodynamics Research),” *71st International Astronautical Congress (IAC)*, 2020. URL <http://hdl.handle.net/2117/330162>.

- [34] Walker, A., Mehta, P., and Koller, J., “Drag Coefficient Model Using the Cercignani–Lampis–Lord Gas–Surface Interaction Model,” *Journal of Spacecraft and Rockets*, Vol. 51, No. 5, 2014, pp. 1544–1563. <https://doi.org/10.2514/1.A32677>, URL <http://arc.aiaa.org/doi/10.2514/1.A32677>.
- [35] Walsh, J. A., and Berthoud, L., “Reducing spacecraft drag in Very Low Earth Orbit through shape optimisation,” *7th European Conference for Aeronautics and Aerospace Sciences (EUCASS)*, 2017, pp. 1–9. <https://doi.org/10.13009/EUCASS2017-449>.
- [36] Park, J. H., Myong, R. S., Kim, D., and Baek, S. W., “Aerodynamic shape optimization of space vehicle in very-low-earth-orbit,” *29th International Symposium on Rarefied Gas Dynamics*, Vol. 1331, No. 2014, 2014. <https://doi.org/http://dx.doi.org/10.1063/1.4902745>, URL <http://aip.scitation.org/doi/abs/10.1063/1.4902745>.
- [37] Crisp, N. H., Roberts, P. C. E., Livadiotti, S., Macario Rojas, A., Oiko, V. T. A., Edmondson, S., Haigh, S. J., Holmes, B. E. A., Sinpetru, L. A., Smith, K. L., Becedas, J., Domínguez, R. M., Sullioti-Linner, V., Christensen, S., Nielsen, J., Bisgaard, M., Chan, Y. A., Fasoulas, S., Herdrich, G. H., Romano, F., Traub, C., García-Almiñana, D., Rodríguez-Donaire, S., Sureda, M., Kataria, D., Belkouchi, B., Conte, A., Seminari, S., and Villain, R., “In-orbit aerodynamic coefficient measurements using SOAR (Satellite for Orbital Aerodynamics Research),” *Acta Astronautica*, Vol. 180, No. October 2020, 2021, pp. 85–99. <https://doi.org/10.1016/j.actaastro.2020.12.024>, URL <https://doi.org/10.1016/j.actaastro.2020.12.024>.
- [38] Rheinfurth, M. H., and Carroll, S. N., “Space Station Rotational Equations of Motion,” Tech. rep., National Aeronautics and Space Administration (NASA), 1985.
- [39] MathWorks, “Aerospace Toolbox (TM), User’s Guide (R2019a),” , 2019.
- [40] Vallado, D. A., *Fundamentals of Astrodynamics and Applications*, fourth edi ed., 9, Microcosm Press/Springer, 2013. <https://doi.org/10.1017/CBO9781107415324.004>.
- [41] Sinpetru, L. A., Crisp, N. H., Mostaza-Prieto, D., Livadiotti, S., and Roberts, P. C. E., “ADBSat: Methodology of a novel panel method tool for aerodynamic analysis of satellites,” *Submitted to Computer Physics Communications*, Vol. TBD, No. TBD, 2021.
- [42] Wie, B., Weiss, H., and Arapostathis, A., “Quaternion feedback regulator for spacecraft eigenaxis rotations,” *Journal of Guidance, Control, and Dynamics*, Vol. 12, No. 3, 1989, pp. 375–380. <https://doi.org/10.2514/3.20418>.
- [43] Bang, H., Tahk, M., and Choi, H., “Large angle attitude control of spacecraft with actuator saturation,” *Control Engineering Practice*, Vol. 11, No. 9, 2003, pp. 989–997. [https://doi.org/10.1016/S0967-0661\(02\)00216-2](https://doi.org/10.1016/S0967-0661(02)00216-2).
- [44] Hedin, A. E., Fleming, E. L., Manson, A. H., Schmidlin, F. J., Avery, S. K., Clark, R. R., Franke, S. J., Fraser, G. J., Tsuda, T., Vial, F., and Vincent, R. A., “Empirical wind model for the upper, middle and lower atmosphere,” *Journal of Atmospheric and Terrestrial Physics*, Vol. 58, No. 13, 1996, pp. 1421–1447. [https://doi.org/10.1016/0021-9169\(95\)00122-0](https://doi.org/10.1016/0021-9169(95)00122-0).
- [45] Wertz, J. R., *Spacecraft Attitude Determination And Control*, Kluwer Academic Publishers, 1999. <https://doi.org/10.1007/978-94-009-9907-7>.

- [46] Markley, F. L., and Crassidis, J. L., *Fundamentals of spacecraft attitude determination and control*, Springer, 2014. <https://doi.org/10.1007/978-1-4939-0802-8>.
- [47] Heidecker, A., “Development of algorithms for attitude determination and control of the AsteroidFinder satellite,” , 2009. URL <https://elib.dlr.de/106988/>.
- [48] Doornbos, E., “Thermospheric Density and Wind Determination from Satellite Dynamics,” Ph.D. thesis, Technische Universiteit Delft, 2011. <https://doi.org/10.1017/CBO9781107415324.004>.